



## ***Ab initio* up to the melting point: Anharmonicity and vacancies in aluminum**

B. Grabowski, L. Ismer, T. Hickel, and J. Neugebauer

*Max-Planck-Institut für Eisenforschung GmbH, D-40237 Düsseldorf, Germany*

(Received 23 December 2008; published 13 April 2009)

We propose a fully *ab initio* based integrated approach to determine the volume and temperature dependent free-energy surface of nonmagnetic crystalline solids up to the melting point. The approach is based on density-functional theory calculations with a controlled numerical accuracy of better than 1 meV/atom. It accounts for all relevant excitation mechanisms entering the free energy including electronic, quasiharmonic, anharmonic, and structural excitations such as vacancies. To achieve the desired accuracy of  $<1$  meV/atom for the anharmonic free-energy contribution without losing the ability to perform these calculations on standard present-day computer platforms, we develop a numerically highly efficient technique: we propose a hierarchical scheme—called upsampled thermodynamic integration using Langevin dynamics—which allows for a significant reduction in the number of computationally expensive *ab initio* configurations compared to a standard molecular dynamics scheme. As for the vacancy contribution, concentration-dependent pressure effects had to be included to achieve the desired accuracy. Applying the integrated approach gives us direct access to the free-energy surface  $F(V, T)$  for aluminum and derived quantities such as the thermal expansion coefficient or the isobaric heat capacity and allows a direct comparison with experiment. A detailed analysis enables us to tackle the long-standing debate over which excitation mechanism (anharmonicity vs vacancies) is dominant close to the melting point.

DOI: [10.1103/PhysRevB.79.134106](https://doi.org/10.1103/PhysRevB.79.134106)

PACS number(s): 63.20.Ry, 65.40.Ba

### **I. MOTIVATION**

At elevated temperatures, the heat capacity of metals significantly deviates from the behavior predicted within the perfect harmonic lattice model. This was pointed out almost 90 years ago in a seminal work by Born and Brody.<sup>1</sup> In this and in many subsequent studies, various mechanisms such as the thermal expansion, the occurrence of anharmonicity, the electronic degrees of freedom,<sup>1</sup> or the formation of vacancies<sup>2</sup> have been proposed to explain the deviations from harmonicity. Recently, *ab initio* calculations for a wide range of metals showed that the predominant part of these deviations can be explained on the basis of quasiharmonic and electronic excitations.<sup>3</sup> However, the *subtle* balance between further contributions, such as explicit anharmonicity (i.e., the explicit dependence of phonons on temperature) and vacancies, could not be clarified so far even for simple elementary metals.<sup>4</sup>

Aluminum is a prototypical example. It has been studied intensively in the past decades due to its industrial importance (light weight, corrosion resistance) and the availability of single crystals. Measuring the high temperature heat capacity, however, turns out to be a challenge and despite numerous measurements using various techniques the obtained data scatter largely.<sup>2,5–15</sup> A quantitative assessment of the subtle influences to the free energy/heat capacity has therefore been considerably hampered. A brief summary of the corresponding literature shall illustrate this fact: initially, the contribution to the high temperature heat capacity due to thermally activated vacancies was believed to exceed the anharmonic contribution and to cause a nonlinear temperature dependence.<sup>2</sup> In 1968, Brooks and Bingham<sup>5</sup> measured the heat capacity of aluminum using dynamic adiabatic calorimetry. Reducing the experimental heat capacity from constant pressure to fixed volume and employing a Debye model, the

authors interpreted the nonlinear increase in their experimental data as arising mainly from explicit anharmonicity. In 1985, Ditmars *et al.*<sup>6</sup> measured the enthalpy of aluminum by means of isothermal phase-change calorimetry and Shukla *et al.*<sup>16</sup> calculated from these results the isobaric heat capacity. Shukla *et al.*<sup>16</sup> then employed the same reduction scheme as Brooks and Bingham<sup>5</sup> to obtain the fixed volume heat capacity. In a subsequent theoretical analysis, they went beyond the Brooks-Bingham approach<sup>5</sup> by employing empirical potentials rather than a simple Debye model to calculate the fixed volume heat capacity. The comparison of the experimental and theoretical data suggested that, in contrast to the original work by Brooks and Bingham,<sup>5</sup> the vacancy contribution dominates the anharmonicity. More recently, in 2004, Forsblom *et al.*<sup>17</sup> calculated the explicit anharmonicity contribution to the fixed volume heat capacity employing an embedded atom method. Their results show, in contrast to the study by Shukla *et al.*,<sup>16</sup> that the contribution due to explicit anharmonicity can well be of a magnitude similar to the one obtained for the vacancy contribution by Shukla *et al.*<sup>16</sup> The precise value could not be assessed since it varied significantly between the used potential parametrizations.<sup>18</sup>

In order to resolve the ongoing controversy and to identify the key mechanisms, two critical issues have to be addressed. (a) First, all previous theoretical studies have been restricted to fixed volume calculations. This assumption constitutes a serious limitation since it requires the use of the above mentioned reduction scheme<sup>5,16,17</sup> in order to compare to experimental data at constant pressure. This reduction involves model assumptions and experimental input parameters such as the temperature dependent bulk modulus, the thermal expansion, and the thermal expansion coefficient. Such an approach is therefore a potential source for uncontrolled errors or error cancellation. (b) Second, all previous

studies were based on a simple Debye model or on empirical potentials. Forsblom *et al.*<sup>17</sup> employed embedded atom potentials fitted to ground state *ab initio* and/or low-temperature experimental data. As a consequence, such potentials are optimized for equilibrium geometries: it is thus not *a priori* clear if their high temperature performance is sufficient to separate the subtle differences between anharmonic and vacancy contributions. In fact, the results of Forsblom *et al.*<sup>17</sup> indicate that the presently available empirical potentials might fail in this respect.<sup>18</sup>

The aim of the present study is to overcome both limitations. For that purpose, we develop an integrated approach which allows us to calculate the complete volume and temperature dependent free-energy surface of aluminum using density-functional theory (DFT). The explicitly calculated volume dependence provides access to properties at constant pressure, which corresponds to the typical experimental condition, and the *ab initio* approach allows for an unbiased parameter-free derivation of the desired quantities. Specifically, we computed the free-energy surface  $F(V, T)$  including

$$F = F^{\text{el}} + F^{\text{qh}} + F^{\text{ah}} + F^{\text{vac}}, \quad (1)$$

with the explicit consideration of the volume,  $V$ , and temperature,  $T$ , dependence for each term. In Eq. (1),  $F^{\text{el}} + F^{\text{qh}}$  is the “standard” contribution which consists of the electronic  $F^{\text{el}}$  and quasiharmonic  $F^{\text{qh}}$  free energy and which has been investigated intensively, e.g., in Ref. 3. To master the challenge of calculating an *ab initio* anharmonic free-energy surface  $F^{\text{ah}}(V, T)$ , we develop a hierarchical scheme to coarse grain the configuration space from  $\approx 10^7$  configurations to  $\approx 10^2$  configurations retaining *ab initio* accuracy (Sec. II C 2). The vacancy contribution  $F^{\text{vac}}(V, T)$  is treated including the full spectrum of excitations—electronic, quasiharmonic, and anharmonic—and without making the common assumption of a constant vacancy volume (Sec. II D 1).

## II. METHODOLOGY

### A. Computational details

The calculations were performed using a plane-wave pseudopotential method as implemented in ABINIT<sup>19,20</sup> and S/PHI/NX<sup>21,22</sup> employing identical pseudopotentials. We used a norm-conserving pseudopotential generated with FHI98PP<sup>23</sup> employing the Hamann<sup>24</sup> construction scheme. The  $3s$  and  $3p$  electrons were treated as valence electrons. Cutoff radii of 1.25 and 1.40 bohr radius were used for the  $s$  and  $d$  components of the generalized-gradient-approximation (GGA) pseudopotential. The remaining  $p$  component and all the components of the local-density-approximation (LDA) pseudopotential were constructed using the default cutoff radii of FHI98PP. The  $d$  component was used as a local orbital. The quality of the pseudopotential was checked against the projector-augmented-wave (PAW) method<sup>25</sup> as implemented in VASP<sup>26,27</sup> and against the all-electron method (augmented plane wave plus local orbitals [(L)APW+lo]) as implemented in WIEN2K.<sup>28</sup> Generally, we find a good agreement between physical properties based on our pseudopotential and the PAW/all-electron approach. Details will be discussed

TABLE I. The used plane-wave cutoffs  $E^{\text{cut}}$  and  $k$  point (kp) densities for the electronic free-energy contributions  $E^{\text{tot}}$  and  $\bar{F}^{\text{el}}$  [defined in Eq. (3)], the quasiharmonic,  $F^{\text{qh}}$ , and explicitly anharmonic,  $F^{\text{ah}}$ , contribution. Example  $k$  meshes corresponding to a one atom unit cell are also given.

	$E^{\text{cut}}$ (Ry)	$k$ -point density (kp-atom)	$k$ mesh for a one atom cell
$E^{\text{tot}}$	14	186624	$57 \times 57 \times 57$
$\bar{F}^{\text{el}}$	14	3014284	$144 \times 144 \times 144$
$F^{\text{qh}}$	34	46656	$36 \times 36 \times 36$
$F^{\text{ah}}$	14	2048	$13 \times 13 \times 13$

in Secs. II B–II D. For the exchange-correlation (XC) functional, LDA as well as GGA were considered. We applied the scheme of Ceperley-Alder<sup>29</sup> as parametrized by Perdew and Zunger<sup>30</sup> for LDA and Perdew *et al.*<sup>31</sup> for GGA.

The plane-wave cutoff and the  $k$  sampling were adjusted for each free-energy contribution separately to guarantee converged results while keeping the computational time as low as possible. The used values are compiled in Table I. Details regarding the extensive convergence checks are given in Secs. II B–II D. For the purpose of testing the convergence, the expansion coefficient  $\alpha$  and the isobaric heat capacity  $C_p$ ,

$$\alpha = \frac{1}{a(T)} \frac{\partial a(T)}{\partial T}, \quad C_p = -T \left( \frac{\partial^2 F(V, T)}{\partial T^2} \right)_{V, P}, \quad (2)$$

with the lattice constant  $a(T)$  and pressure  $P$ , are found to be the most sensitive physical target properties.

### B. $T=0$ K properties, electronic excitations, and quasiharmonic approximation

The representation of the electronic free energy  $F^{\text{el}}$  becomes particularly convenient if it is divided into the total energy  $E^{\text{tot}}(V)$  at  $T=0$  K and a remaining part  $\bar{F}^{\text{el}}$ ,

$$F^{\text{el}}(V, T) = E^{\text{tot}}(V) + \bar{F}^{\text{el}}(V, T). \quad (3)$$

We investigated three different equations of state (EOSs) as a parametrization of  $E^{\text{tot}}(V)$ : the Murnaghan EOS,<sup>32</sup> its extension the third-order Birch-Murnaghan EOS,<sup>33</sup> and the Vinet EOS.<sup>34</sup> The Vinet EOS (Ref. 34) has been found to describe theoretical and experimental curves of various materials most accurately.<sup>35</sup> For the  $C_p$  in our material system, we find negligible<sup>36</sup> differences between the three EOSs. For  $\alpha$ , the Birch-Murnaghan and Vinet EOSs yield a similar value which is, however, 1.9% larger<sup>37</sup> than the one obtained using the Murnaghan EOS. We ascribe this to the improved nature of the Birch-Murnaghan and Vinet EOSs. For the further analysis, we use the Vinet EOS.

The  $T=0$  K bulk properties obtained from  $E^{\text{tot}}(V)$  for our LDA and GGA pseudopotential are compared to the corresponding PAW and all-electron quantities in Table II. The overall agreement is good. The difference in the lattice constant and bulk modulus gives rise to a smaller (larger)<sup>37</sup>  $\alpha$  of

TABLE II.  $T=0$  K properties excluding zero-point vibrations ( $V_{\text{eq}}$ : equilibrium volume per atom;  $B_{\text{eq}}$ : bulk modulus at  $V_{\text{eq}}$ ; and  $B'_{\text{eq}}$ : derivative of  $B_{\text{eq}}$  with respect to pressure).

LDA	$V_{\text{eq}}$ ( $\text{\AA}^3$ )	$B_{\text{eq}}$ (GPa)	$B'_{\text{eq}}$
Pseudopotential	15.62	82	4.6
PAW	15.82	84	4.6
All electron	15.83	83	4.5
GGA	$V_{\text{eq}}$ ( $\text{\AA}^3$ )	$B_{\text{eq}}$ (GPa)	$B'_{\text{eq}}$
Pseudopotential	16.61	75	4.6
PAW	16.50	78	4.7
All electron	16.52	77	4.7

–2.1% (4.8%) and  $C_p$  of –1.2% (1.4%) for LDA (GGA) with respect to the all-electron results. In principle the all-electron  $T=0$  K energetics could be used for the further analysis. However, for a determination of the vacancy contribution, it is necessary to ensure an overall consistency and to resort to the pseudopotential  $T=0$  K energetics. The deviations do not affect the results for the anharmonic contribution.

In order to calculate  $\bar{F}^{\text{el}}$ , we employed Mermin’s finite temperature formulation<sup>38</sup> of DFT. We calculated  $\bar{F}^{\text{el}}(V, T)$  on a mesh of seven volumes and nine temperatures in the relevant region: the considered temperature range is (0, ..., 1000) K (melting temperature: 933 K), which in turn determines the relevant volume range:  $V_{\text{eq}}(T=0 \text{ K}), \dots, V_{\text{eq}}(T=1000 \text{ K})$ , where  $V_{\text{eq}}(T=0 \text{ K})$  is the equilibrium volume at  $T=0$  K as given in Table II, and  $V_{\text{eq}}(T=1000 \text{ K}) \approx 1.1V_{\text{eq}}(T=0 \text{ K})$  is the equilibrium volume at  $T=1000$  K. We further used a two-dimensional fourth-order polynomial ( $\sum_{i,j} V^i T^j$  with  $i \geq 0$ ,  $j \geq 1$ , and  $i+j \leq 4$ ) to parametrize  $\bar{F}^{\text{el}}$  as a function of  $V$  and  $T$ . Due to the highly converged  $k$  mesh (see Table I), the calculated  $\bar{F}^{\text{el}}$  values have a smooth dependence on both variables. This enables a convergence with respect to the order of the fitting polynomial. Inclusion of terms beyond the fourth order does not yield any significant improvement to the fit.<sup>36</sup>

The quasiharmonic contribution  $F^{\text{qh}}$  was calculated using the linear response method.<sup>39,40</sup> Since in the considered system only a one atom cell is needed for the calculation of phonons, this approach allows testing the  $k$  and plane-wave cutoff convergence even for extremely high values. A “high” quality convergence for this contribution is necessary since the quasiharmonic phonons determine the largest part of the free energy. Small errors in the phonons can significantly alter the free energy at high temperatures. A well-defined quasiharmonic free energy is however crucial for determining the anharmonic free energy. The converged values are given in Table I. The phonons were calculated at  $q$  points corresponding to (in units of the cubic four-atom fcc unit cell) a  $2^3$  (=32 atoms), a  $3^3$  (=108 atoms), and a  $4^3$  (=256 atoms) supercell. Each of the  $q$  meshes was Fourier transformed onto a dense converged  $q$  mesh consisting

of  $m^3$  mesh points ( $m=16$ ) from which  $F^{\text{qh}}$  was calculated using<sup>41</sup>

$$F^{\text{qh}}(T) = \frac{1}{m^3} \sum_q^{3m^3} \left\{ \frac{\hbar \omega_q}{2} + k_B T \ln \left[ 1 - \exp\left(-\frac{\hbar \omega_q}{k_B T}\right) \right] \right\}. \quad (4)$$

Here,  $\hbar$  is the reduced Planck constant,  $k_B$  is the Boltzmann constant, and  $\omega_q$  are the phonon frequencies, with  $q$  running over the  $m^3$  mesh points and over the three branches for each mesh point. The free energy  $F^{\text{qh}}$  in Eq. (4) is implicitly volume dependent due to the explicitly calculated volume dependence of the frequencies. We calculated  $F^{\text{qh}}$  at seven different volumes in the relevant range. The parametrization of the  $V$  dependence is discussed in Sec. III A. Increasing the supercell from  $2^3$  to  $3^3$  leads to a decrease in  $\alpha$  by –4.4% and  $C_p$  by –1.6%.<sup>37</sup> A further increase in the supercell yields only negligible<sup>36</sup> effects. Hence, in the further analysis a  $q$  mesh corresponding to a  $3^3$  supercell will be used.

### C. Explicit anharmonicity

#### 1. Thermodynamic integration

In order to compute the explicitly anharmonic free energy,  $F^{\text{ah}}$ , which corresponds to the difference between the full vibrational free energy and the quasiharmonic contribution  $F^{\text{qh}}$ , a statistical approach was employed. Specifically, we used the concept of thermodynamic integration<sup>22,42,43</sup> according to which  $F^{\text{ah}}$  reads

$$F^{\text{ah}}(V, T) = \int_{\lambda=0}^{\lambda=1} d\lambda \left( \frac{\partial F(V, T, \lambda)}{\partial \lambda} \right). \quad (5)$$

Here,  $F(V, T, \lambda)$  denotes the free energy along a thermodynamic path connecting the quasiharmonic with the full vibrational (quasiharmonic + anharmonic) state by means of a coupling parameter  $\lambda$ . To parametrize this thermodynamic path, we chose a linear interpolation between the quasiharmonic  $U^{\text{qh}}$  and the full vibrational potential  $U^{\text{qh+ah}}$ ,

$$U(\lambda) = (1 - \lambda)U^{\text{qh}} + \lambda U^{\text{qh+ah}}. \quad (6)$$

The quantity  $\partial F(V, T, \lambda) / \partial \lambda$  was determined from a canonical ensemble average,

$$\partial F(V, T, \lambda) / \partial \lambda = \langle \partial U(\lambda) / \partial \lambda \rangle_{\lambda}. \quad (7)$$

To produce a proper canonical ensemble for a given  $\lambda$  value, we performed Langevin dynamics<sup>22</sup> simulations with a time step of 10 fs. The number of molecular dynamics (MD) steps was adjusted to the specific volume, temperature, and supercell size, such as to achieve a standard deviation of less than 1 meV/atom. Our largest simulations consisted of  $\approx 10\,000$  MD steps.

We investigated the  $\lambda$  dependence in detail for the perfect bulk and vacancy calculations. In particular, we studied the  $\lambda$  dependence at extreme conditions, such as temperatures close to the melting point, sufficiently large volumes, and  $\lambda$  values close to 0 and 1. Specifically, we computed a dense set of  $\lambda$  values at 900 K for a small and a large volume for both the perfect bulk and the vacancy cell. The results, shown in Fig. 1, reveal that the perfect bulk and the vacancy

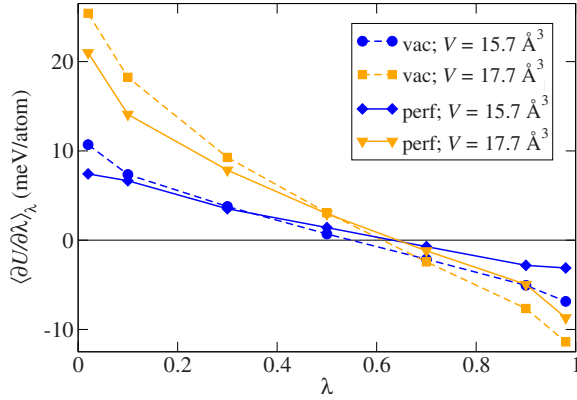


FIG. 1. (Color online)  $\lambda$  dependence of the ensemble average quantity  $\langle \partial U / \partial \lambda \rangle_\lambda$  for the perfect (perf) bulk and vacancy (vac) calculations for a small and a large volume each. The results were obtained for a  $2^3$  supercell, the LDA functional, and a temperature of 900 K. The standard deviations (Ref. 44) ( $\approx 0.5$  meV/atom) are of a similar size as the symbols indicating the calculated values. The solid and dashed lines are guides for the eyes.

cell show nearly the same  $\lambda$  dependencies. Moreover, we see, even at this high temperature, only negligible deviations from linearity for the smaller volume. For the larger volume, deviations are found for  $\lambda$  values close to 0 and 1, which partially compensate each other. The consequence of the increase in the number of  $\lambda$  values in the integration in Eq. (5) is shown in Fig. 2. For the larger volume, the free energy obtained from an integration based on the dense  $\lambda$  sampling ( $\lambda$  set 2 in Fig. 2) is 0.9 meV/atom higher than one based on  $\lambda=0.5$  only. Since the free energy at the smaller volume does not change upon inclusion of more  $\lambda$  values, we observe in total a small positive shift in the slope of the  $F^{\text{ah}}(V)$  curve.

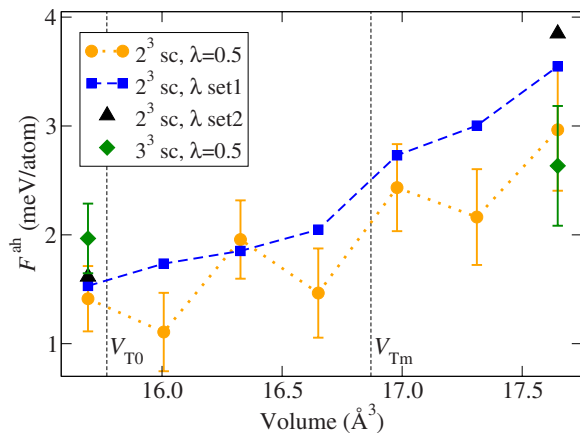


FIG. 2. (Color online) Explicitly anharmonic free energy  $F^{\text{ah}}$  at 900 K for the LDA functional. Results for the  $2^3$  and  $3^3$  supercell (sc) and for three different  $\lambda$  samplings,  $\lambda=0.5$ ,  $\lambda$  set 1 =  $\{0.1, 0.3, 0.5, 0.7, 0.9\}$ , and  $\lambda$  set 2 = set 1 +  $\{0.02, 0.98\}$ , used for the integration in Eq. (5) are shown. The symbols represent the calculated values, the corresponding vertical lines show the standard deviation (Ref. 44), and the dashed and dotted lines in between are guides for the eyes. The vertical black dashed lines indicate the 0 K (including zero-point vibrations) and the melting temperature equilibrium volumes of LDA,  $V_{T0}$  and  $V_{Tm}$ , respectively.

This shift decreases  $\alpha$  by  $-1.6\%$  and  $C_p$  by  $-0.6\%$ .<sup>37</sup> These changes are opposite to the changes (2.1% for  $\alpha$  and 0.8% for  $C_p$ ) caused by the negative shift of the slope of  $F^{\text{ah}}(V)$ , which occurs when the supercell size is increased from  $2^3$  to  $3^3$  (see Fig. 2). For the further analysis, we use the  $2^3$  supercell at  $\lambda=0.5$ .

## 2. Developing an efficient scheme to coarse grain the configuration space: The upsampled thermodynamic integration using Langevin dynamics approach

The main challenge in calculating  $F^{\text{ah}}$  from *ab initio* arises from long computational times. To illustrate this, let us consider an average calculation for a  $2^3$  supercell ( $=32$  atoms). To achieve the desired accuracy, a direct sampling of the phase space using MD would require  $\approx 10^7$  MD steps. This is consistent with the number given in Ref. 17, where  $10^6$  MD steps were found to be sufficient for a larger supercell (500 atoms). With increasing number of atoms in the supercell, the spatial averaging improves reducing the number of MD steps. A reduction from  $\approx 10^7$  MD steps to  $\approx 10^4$  can be achieved by applying the thermodynamic integration approach described in Sec. II C 1. This number is however still too large for a direct *ab initio* sampling: for reasonably converged parameters ( $4^3 k$  mesh, 2048  $k$ -point (kp)-atom, and 14 Ry plane-wave cutoff; see Table I), a single MD step takes approximately one CPU hour<sup>45</sup> and hence a complete MD run takes several thousand CPU hours. This number needs to be multiplied by the number of  $F^{\text{ah}}(V, T)$  points needed to obtain a reasonable parametrization for the  $F^{\text{ah}}$  surface ( $\approx 30, \dots, 40$  points). Taking into account additional convergence checks especially for the supercell size, such a study rapidly exceeds today's available CPU contingents.

In order to overcome these difficulties, we propose the following procedure which we refer to as the upsampled thermodynamic integration using Langevin dynamics (UP-TILD) method and which provides an efficient hierarchical scheme to coarse grain the configuration space: as a first step, we perform a thermodynamic integration MD run (referred to as first run in the following) as described in Sec. II C 1 on a rather low-converged set of parameters ( $2^3 k$  mesh, 256 kp-atom, and 8 Ry plane-wave cutoff). This reduces the time for a MD step down to  $\approx 120$  s, i.e., a gain by a factor of  $\approx 30$  compared to a calculation using well-converged parameters. With this time reduction, the first run can be easily extended to several thousand steps in order to obtain the desired statistical accuracy. The convergence of  $\langle \partial U / \partial \lambda \rangle_\lambda^{\text{low}}$  (the superscript indicates a reference to the set of low-converged parameters) for such a calculation is shown in Fig. 3(a). Due to the reduction in the convergence parameters, we have however a significant loss of accuracy. To correct this, we calculate in a second step the difference  $\Delta E$  between the energy  $E^{\text{low}}$  and  $E^{\text{high}}$  for a set of low- and high-converged parameters, respectively. We therefore take a set  $\{\mathbf{R}_I\}_u$  of uncorrelated MD structures from the first run, with  $\mathbf{R}_I$  as the coordinates of atom  $I$ ,  $u=1, \dots, M$ , and  $M$  as the number of MD structures in the set. We then calculate the energies for these  $M$  structures with the low and high converged parameter set and take the average of their difference,

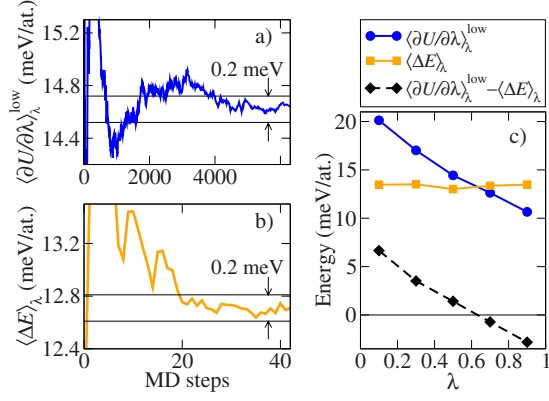


FIG. 3. (Color online) Illustration of the UP-TILD method. (a) Convergence of the average quantity  $\langle \partial U / \partial \lambda \rangle_\lambda^{\text{low}}$  (at  $V = 15.7 \text{ \AA}^3$ ,  $T = 900 \text{ K}$ , and  $\lambda = 0.5$ ) as a function of the number of MD steps for a “usual” thermodynamic integration run as discussed in Sec. II C 1. The superscript indicates that the run is performed with low-converged parameters. (b) Convergence of the average energy difference  $\langle \Delta E \rangle_\lambda$  for a set of uncorrelated MD structures taken from the run in (a). The difference is obtained from the low and high converged energies according to Eq. (8). (c) The  $\lambda$  dependence of the converged quantities from (a) and (b) and their difference  $\langle \partial U / \partial \lambda \rangle_\lambda^{\text{low}} - \langle \Delta E \rangle_\lambda = \langle \partial U / \partial \lambda \rangle_\lambda^{\text{high}}$ , which corresponds to the upsampled quantity  $\langle \partial U / \partial \lambda \rangle_\lambda^{\text{high}}$ , are shown.

$$\langle \Delta E \rangle_\lambda = \frac{1}{M} \sum_{u=1}^M (E_u^{\text{low}} - E_u^{\text{high}}). \quad (8)$$

The energies  $E_u^{\text{low}}$  and  $E_u^{\text{high}}$  are referenced with respect to their corresponding equilibrium energies,

$$E_u^c = E_u^{c,\text{tot}} - E_{\text{eq}}^c, \quad \text{with } c = \text{low, high}. \quad (9)$$

Here,  $E_u^{c,\text{tot}}$  is the total energy of the  $u$ th MD structure and  $E_{\text{eq}}^c$  is the total energy of the system with all atoms at their equilibrium position. The energies  $E_u^{c,\text{tot}}$  are implicitly  $\lambda$ , volume, and temperature dependent, whereas  $E_{\text{eq}}^c$  is only volume dependent and can be considered as corresponding to  $T = 0 \text{ K}$ .

An example for the convergence of  $\langle \Delta E \rangle_\lambda$  defined in Eq. (8) is shown in Fig. 3(b) and demonstrates the performance of the UP-TILD approach: the convergence rate is improved by about 2 orders of magnitude compared to the original one for  $\langle \partial U / \partial \lambda \rangle_\lambda$  keeping the number of the computationally expensive calculations  $E_u^{\text{high,tot}}$  small. In the last step, the converged quantity  $\langle \partial U / \partial \lambda \rangle_\lambda^{\text{high}}$  is obtained by<sup>46</sup>

$$\langle \partial U / \partial \lambda \rangle_\lambda^{\text{high}} = \langle \partial U / \partial \lambda \rangle_\lambda^{\text{low}} - \langle \Delta E \rangle_\lambda. \quad (10)$$

An example for the upsampling at different  $\lambda$  values is shown in Fig. 3(c). It demonstrates a further advantage of the UP-TILD method: the  $\lambda$  dependence of  $\langle \Delta E \rangle_\lambda$  becomes negligible. It is therefore a good approximation to neglect it completely and work with a single  $\langle \Delta E \rangle_\lambda$  at some fixed  $\lambda$ .

In order to verify that the UP-TILD approach is applicable to our material system, we calculated  $\langle \partial U / \partial \lambda \rangle_\lambda^{\text{high}}$  directly and by means of Eq. (10). A representative set of results is shown in Fig. 4.

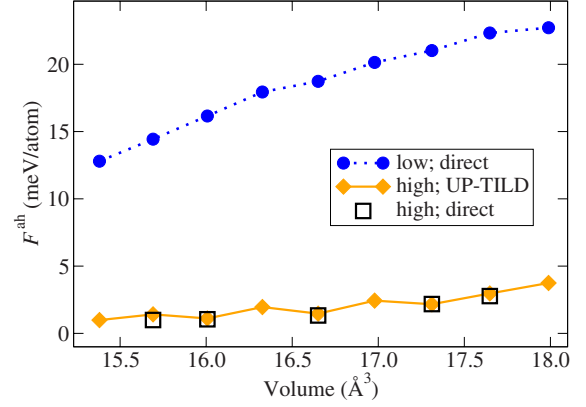


FIG. 4. (Color online) Explicitly anharmonic free energy  $F^{\text{ah}}$  at 900 K for the LDA functional and the  $2^3$  supercell. Results for low and high converged parameters are shown: low: 8 Ry, 256 kp-atom and high: 14 Ry, 2048 kp-atom. Free energies obtained directly from a usual thermodynamic integration calculation are marked as “direct,” while “UP-TILD” indicates that the UP-TILD method was employed.

The figure illustrates the good performance of the method. The directly calculated values agree to within the statistical uncertainty with the upsampled values and reproduce the volume dependence of  $F^{\text{ah}}$  accurately. Moreover, Fig. 4 shows that it is indeed crucial to use the set of well-converged parameters since the set of low-converged parameters yields both substantial deviations in the absolute values and an incorrect volume dependence.

A prerequisite for the UP-TILD approach to be applicable is that the phase spaces spanned by the set of low and high converged parameters are sufficiently similar and that the difference can be described by a nearly constant energy shift. If the phase spaces differ significantly, the method will not be applicable. To check whether or not the UP-TILD method will work, a small set of  $F^{\text{ah}}$  points may be computed and compared to the upsampled values as shown in Fig. 4. Such an explicit test, however, is computationally demanding. We therefore suggest two implicit criteria. (a) If the two phase spaces are similar,  $\langle \Delta E \rangle_\lambda$  will be nearly independent of  $\lambda$  [see Fig. 3(c)]. Hence, deviations from this independence can be used as a measure of the similarity of the phase spaces. (b) An alternative measure is the number of structures needed to obtain a converged  $\langle \Delta E \rangle_\lambda$  for a single  $\lambda$  value.

### 3. Convergence issues

The UP-TILD method can be easily extended to a hierarchical scheme which allows to further improve the convergence of the DFT calculations and/or to improve the statistical sampling. To illustrate this, let us consider a convergence series with a set of values  $\{x_1, x_2, x_3\}$  with successively increasing quality and computational expense:  $x_1 < x_2 < x_3$ . The upsampling is performed for  $x_1$  and  $x_2$  as described above. The upsampling for  $x_3$  is now performed with respect to  $x_2$  and not  $x_1$ , i.e., we calculate  $\langle \Delta E \rangle_\lambda^{2 \rightarrow 3} = 1/M' \sum_u^{M'} (E_u^{x_2} - E_u^{x_3})$ . This quantity converges even faster than  $\langle \Delta E \rangle_\lambda^{1 \rightarrow 2} = 1/M \sum_u^M (E_u^{x_1} - E_u^{x_2})$ , i.e.,  $M' \ll M$ , and

therefore further reduces the expensive calculations corresponding to  $x_3$ . Using this approach, Eq. (10) has to be replaced by

$$\langle \partial U / \partial \lambda \rangle_{\lambda}^{\text{high}} = \langle \partial U / \partial \lambda \rangle_{\lambda}^{\text{low}} - \langle \Delta E \rangle_{\lambda}^{1-2} - \langle \Delta E \rangle_{\lambda}^{2-3}. \quad (11)$$

This scheme can be easily extended to higher hierarchies.

Applying this procedure, we investigated the convergence of the plane-wave cutoff and  $k$  mesh for a selected set of volumes and temperatures on the anharmonic free-energy surface. To achieve a high accuracy, it is important to choose high temperatures (i.e., close to the melting temperature). The corresponding atomic configurations represent the most distorted structures, which in turn are the most sensitive with respect to the convergence parameters. As for the volume, at least two points have to be investigated to obtain the influence on the thermodynamic properties. Based on these considerations, we find that a cutoff of 14 Ry and a  $k$  sampling of 2048  $k$ -atom are sufficient. It is interesting to compare these values to the converged parameters for the quasiharmonic contribution (34 Ry and 46 656  $k$ -atom; see Table I): the anharmonic contribution converges considerably faster than the quasiharmonic one. The reason is that the anharmonic contribution is based directly on the energy, whereas the quasiharmonic one relates to the second derivative in the potential energy surface.

A further advantage of the hierarchical UP-TILD approach is the possibility to easily check the pseudopotential anharmonic free energy against, for instance, alternative DFT implementations such as PAW or all-electron calculations. To illustrate this feature, we calculated  $\langle \Delta E \rangle_{\lambda}^{\text{pp} \rightarrow \text{PAW}} = 1/M \sum_u^M (E_u^{\text{pp}} - E_u^{\text{PAW}})$ , where  $E_u^{\text{pp}}$  is the pseudopotential energy and  $E_u^{\text{PAW}}$  is the PAW energy of the  $u$ th MD structure. Note that due to Eq. (9) there are no total energy contributions from the pseudopotential and PAW potential. We find here again that pseudopotential and PAW results agree very well, i.e., that  $\langle \Delta E \rangle_{\lambda}^{\text{pp} \rightarrow \text{PAW}}$  is small ( $\approx 0.5$  meV/atom at 900 K and  $\lambda=0.5$ ).

#### 4. Challenges in parametrizing the anharmonic free-energy surface

A critical point in calculating derivative quantities such as the expansion coefficient or the heat capacity from an anharmonic free-energy surface is the choice of the parametrization with respect to  $V$  and  $T$ . This problem has three aspects. (a) A technical one: even though tools are available to sample the phase space effectively, reducing the standard deviation to much less than 1 meV/atom quickly becomes computationally prohibitive, especially for high temperatures. Thus, in practice, the anharmonic free-energy surface will contain non-negligible statistical noise. (b) A physical one: despite the statistical noise, we can clearly identify that the temperature dependence of the surface contains higher order contributions at least up to the cubic term (see Figs. 9 and 12). Moreover, our results also suggest that  $V$ - $T$  coupling terms have non-negligible contributions. (c) A fundamental one: in contrast to the temperature dependence of the quasiharmonic free energy [Eq. (4)], no analytical equation for the anharmonic free energy is known.

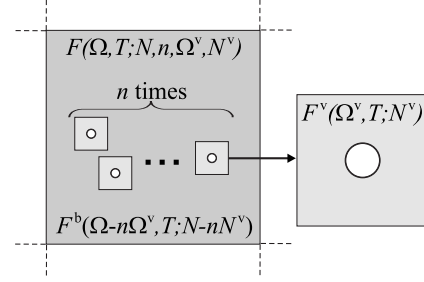


FIG. 5. Schematic illustration of the concept of calculating the free energy  $F(\Omega, T; N, n, \Omega^v, N^v)$  of a periodic crystal with vacancies. The larger box represents a supercell of volume  $\Omega$  at temperature  $T$  containing  $N$  atoms and  $n$  vacancies. A light-gray shaded box with a white circle represents a cell of volume  $\Omega^v$ , containing  $N^v$  atoms, exactly one vacancy, and having the free energy  $F^v(\Omega^v, T; N^v)$ . The dark-gray shaded region represents the perfect bulk without vacancies, with volume  $\Omega - n\Omega^v$ ,  $N - nN^v$  atoms, and free energy  $F^b(\Omega - n\Omega^v, T; N - nN^v)$ . The dashed lines indicate periodic boundary conditions.

Due to the lack of an analytical expression, we have to use a polynomial series to expand  $F^{\text{ah}}(V, T)$ . Based on the discussion above and extensive convergence checks, it became clear that this is critically hindered by the interplay of (a) and (b). To take into account higher orders, we need a sufficiently large polynomial basis. But taking a too large polynomial basis, the parametrization becomes unphysical due to the statistical noise. We will therefore derive in Sec. III B a conceptually different approach which solves this problem.

## D. Vacancies

### 1. Derivation of the volume-optimized free energy of vacancies

In the present section, we derive the vacancy contribution  $F^{\text{vac}}$ . We consider the dilute limit, i.e., vacancy-vacancy interaction is assumed to be negligible. To this end, we provide an intuitive derivation adapted to periodic supercell calculations as frequently employed in *ab initio* studies. We start our derivation with considering a large fictitious, i.e., computationally not accessible, supercell of a periodic crystal at some fixed volume  $\Omega$ , at a temperature  $T$ , containing  $N$  atoms, and  $n$  vacancies. As illustrated in Fig. 5, each vacancy is described by a cell of volume  $\Omega^v$  with  $N^v$  atoms around the vacancy. This cell is in the following referred to as the “vacancy cell.”

It has to be sufficiently large to cover the full strain field of the vacancy. The remaining bulk, with volume  $\Omega^b = \Omega - n\Omega^v$  and  $N^b = N - nN^v$  atoms, contains by definition no vacancy contributions and can, therefore, be described by the perfect bulk. Using these definitions, the free energy of the supercell can be written as

$$F(\Omega, T; N, n, \Omega^v, N^v) = F^b(\Omega^b, T; N^b) + nF^v(\Omega^v, T; N^v) + F^c(N, n). \quad (12)$$

The configurational free energy  $F^c$  of a point defect such as the vacancy reads in Stirling’s approximation,

$$F^c = -k_B T [n - n \ln(n/N)]. \quad (13)$$

In order to avoid the explicit dependence on the number of atoms  $N$  of the fictitious supercell, we rescale Eq. (12) by  $1/N$  and introduce  $V = \Omega/N$  and the vacancy concentration  $c = n/N$ . Additionally, we make use of the fact that the free energy of the perfect bulk  $F^b$  is an extensive quantity,

$$F^b(\Omega^b, T; N^b)/N^b = F^b(V^b, T; 1) = :F^b(V^b, T), \quad (14)$$

with

$$V^b(V, c) = \Omega^b/N^b = (V - c\Omega^v)/(1 - cN^v). \quad (15)$$

The resulting expression

$$\begin{aligned} F(\Omega, T; N, n, \Omega^v, N^v)/N \\ = (1 - cN^v)F^b(V^b, T) + cF^v(\Omega^v, T; N^v) - ck_B T(1 - \ln c) \\ = :F(V, T; c, \Omega^v, N^v) \end{aligned} \quad (16)$$

is independent of  $N$  and defines the free energy per atom  $F(V, T; c, \Omega^v, N^v)$  of the full supercell consisting of the perfect crystal and  $n$  vacancy cells.

The dependence on the initially unknown quantities  $c$  and  $\Omega^v$  is eliminated by enforcing the equilibrium conditions,

$$\partial F(V, T; c, \Omega^v, N^v)/\partial c = 0, \quad (17)$$

$$\partial F(V, T; c, \Omega^v, N^v)/\partial \Omega^v = 0. \quad (18)$$

The first condition ensures that the concentration of vacancies corresponds at each temperature to the thermodynamic equilibrium. The physical origin for Eq. (18) is the simultaneous relaxation of  $\Omega^v$  and  $\Omega^b$  due to the removal of an atom from the vacancy cell and its addition to the perfect crystal. Both volumes need to be optimized under the additional constraint of their mutual coupling  $\Omega^b = \Omega - n\Omega^v$  which enters the definition of  $V^b$ . The remaining unknown quantity  $N^v$  is determined by the specific supercell used for the vacancy calculation and has to be checked for convergence. Solving Eqs. (17) and (18) yields the equilibrium values  $c_{\text{eq}}$  and  $\Omega_{\text{eq}}^v$ . We then get the final expression of the free energy of a crystal with vacancies of volume  $V$  and at a temperature  $T$ ,

$$\begin{aligned} F(V, T) = (1 - c_{\text{eq}}N^v)F^b[V_{\text{eq}}^b(V), T] \\ + c_{\text{eq}}F^v(\Omega_{\text{eq}}^v, T; N^v) - c_{\text{eq}}k_B T(1 - \ln c_{\text{eq}}), \end{aligned} \quad (19)$$

with

$$V_{\text{eq}}^b(V) = (V - c_{\text{eq}}\Omega_{\text{eq}}^v)/(1 - c_{\text{eq}}N^v). \quad (20)$$

We now compare the presented *volume-optimized* approach of calculating thermodynamic properties of vacancies with the commonly applied constant volume approach.<sup>47,48</sup> The latter starts with an approximate expression for the vacancy cell volume,

$$\Omega^v \approx N^v \Omega / N. \quad (21)$$

This implies that  $V^b = V = \Omega/N$  in contrast to the self-consistently determined volume [Eq. (20)]. Using this approximation and the extensive nature of  $F^b$ , Eq. (16) can be rewritten as

$$\begin{aligned} F(V, T; c) = F^b(V, T) - ck_B T(1 - \ln c) \\ + c \left[ F^v \left( \frac{N^v}{N} \Omega, T; N^v \right) - \frac{N^v}{N} F^b(\Omega, T; N) \right] \\ = F^b(V, T) - ck_B T(1 - \ln c) + cF^f(V, T). \end{aligned} \quad (22)$$

Here, the last equality defines the formation free energy  $F^f$ . Setting  $N^v = N - 1$ , we indeed see that our formalism together with approximation Eq. (21) reduces to the well-known expression<sup>47</sup> of the vacancy formation energy. For this approximate case and assuming an equilibrium vacancy concentration a separation of the free energy into a perfect crystal and a vacancy contribution  $F^{\text{vac}}$ ,

$$F(V, T) = F^b(V, T) - k_B T c_{\text{eq}}(V, T) = F^b(V, T) + F^{\text{vac}}(V, T), \quad (23)$$

is possible. In Sec. III C, we compare our approach with the more approximate one given by Eqs. (21) and (22).

It is important to stress that the volume-optimized approach is not equivalent to a constant pressure vacancy calculation.<sup>49</sup> In the latter, a formation free energy is defined and calculated by adjusting the volume  $\Omega^v$  of the vacancy supercell to correspond to the same pressure as obtained for the perfect bulk. In this manner, the vacancy cell and the perfect bulk become coupled, but this coupling is *concentration independent*. It coincides with our approach only if the vacancy concentration within a vacancy supercell is identical to the target vacancy concentration, i.e., only if  $c_{\text{eq}} = 1/N^v$ . In such a case, the factor in front of the  $F^b$  term in Eq. (19) is zero and  $F(V, T)$  becomes independent of  $F^b$ . In most practical cases,  $c_{\text{eq}}$  is orders of magnitude smaller [see, e.g., Fig. 11] than the concentration in a realistic supercell giving rise to an artificial overestimation of the coupling in the constant pressure approach. The constant volume/pressure approaches can be thus regarded as limits for our approach in the extreme dilute limit and in the high concentration limit, respectively.

## 2. Convergence issues

The perfect bulk and vacancy free energies,  $F^b$  and  $F^v$ , entering Eqs. (16)–(19) must both include the various free-energy contributions discussed thus far. To make this issue more clear, it is useful to write out these contributions explicitly and apply Eq. (3),

$$F^b(x) = E^{b,\text{tot}}(V^b) + \bar{F}^{b,\text{el}}(x) + F^{b,\text{qh}}(x) + F^{b,\text{ah}}(x),$$

$$F^v(y) = E^{v,\text{tot}}(\Omega^v; N^v) + \bar{F}^{v,\text{el}}(y) + F^{v,\text{qh}}(y) + F^{v,\text{ah}}(y), \quad (24)$$

with  $x = \{V^b, T\}$  and  $y = \{\Omega^v, T; N^v\}$ .

The  $T=0$  K energies,  $E^{b,\text{tot}}$  and  $E^{v,\text{tot}}$ , were calculated using a  $k$  sampling of 186 624 kp-atom. (The kp densities here and in the following refer to the perfect bulk.) This special value ensures commensurable  $k$  meshes for the  $2^3$  ( $=18^3$   $k$  mesh) and  $3^3$  ( $=12^3$   $k$  mesh) supercells used to describe the vacancy. The  $2^3$  supercell is found to be sufficient.<sup>36</sup> We calculated  $E^{b,\text{tot}}$  and  $E^{v,\text{tot}}$  at seven volumes each. For the

vacancy supercell, all internal atomic coordinates were fully relaxed at each volume. To parametrize the volume dependence, we employed the Vinet equation of state (Sec. II B).

The contribution  $\bar{F}^{b,el}$  has been discussed in detail in Sec. II B. To calculate  $\bar{F}^{v,el}$ , we used a  $2^3$  supercell. The volumes, the temperatures, and the parametrization were chosen to be the same as in the case of  $\bar{F}^{b,el}$ . As for the  $k$  sampling, we investigated three meshes:  $14^3$  (87 808 kp·atom),  $16^3$  (131 072 kp·atom), and  $18^3$  (186 624 kp·atom). We find that the electronic term yields negligible<sup>36</sup> contribution to  $\alpha$  and  $C_P$  for all  $k$  meshes.

The calculation of the quasiharmonic free-energy contributions,  $F^{b,qh}$  and  $F^{v,qh}$ , requires special attention to ensure a consistent treatment of the vacancy supercell with the corresponding bulk part. As outlined in Sec. II B [Eq. (4)], for the bulk system a two step procedure is employed to obtain a sufficiently dense mesh of phonon frequencies. First, the frequencies at the exact  $q$  points for modestly sized ( $2^3$ ,  $3^3$ , or  $4^3$ ) supercells are determined. In a second step, these frequencies are projected on a dense grid via Fourier interpolation. Using this dense grid rather than the sparse grid of exact  $q$  points to sample the Brillouin zone is crucial to obtain the desired accuracy, particularly for the low-temperature case where the relevant phonon states are the acoustic branches close to the  $\Gamma$  point. For modest supercell sizes the only exact  $q$  point in this region is the exact  $\Gamma$  point. Since there, all acoustic branches become exactly zero, the sampling is poor and improves only when going to unrealistically large supercell sizes. The slow convergence can be effectively avoided by going over to a dense mesh which can be easily computed for the bulk cell as discussed above. For a vacancy supercell, however, translational symmetry is no longer preserved making the Fourier interpolation infeasible. To nevertheless treat both terms,  $F^{b,qh}$  and  $F^{v,qh}$ , equivalently, we apply a simple correction scheme. This scheme is based on the fact that the vacancy induced changes in the phonons are localized around the vacancy and will thus exhibit a weak phonon dispersion, i.e., these changes can be well described on a sparse  $q$  mesh. The acoustic branches, in contrast, are spatially delocalized and require thus a high density  $q$  mesh. Based on these observations, we applied the following correction:<sup>50</sup>

$$F(V, T) = \tilde{F}(V, T) - F^{b,qh}(V, T) + F_{\text{mesh}}^{b,qh}(V, T). \quad (25)$$

Here,  $\tilde{F}$  is the free energy obtained from applying Eqs. (16)–(19) to  $F^{b,qh}$  and  $F^{v,qh}$  (which are both calculated on the exact  $q$  mesh of the vacancy supercell), while  $F_{\text{mesh}}^{b,qh}$  is the quasiharmonic free energy of the ideal bulk calculated from a dense Fourier interpolated mesh. To calculate  $F^{v,qh}$ , we used the (direct) force constant method<sup>51</sup> (also referred to as the small displacement method<sup>52,53</sup>) using a positive and negative displacements of  $\pm 0.0053 \text{ \AA}$  ( $\pm 0.01$  bohr radius) to obtain the Hellmann-Feynman forces. We investigated a  $2^3$  supercell with two different  $k$  meshes,  $5^3$  (=4000 kp·atom) and  $6^3$  (=6912 kp·atom) and a  $3^3$  supercell with a  $3^3$   $k$  mesh (=2916 kp·atom). We find negligible<sup>36</sup> differences between all three calculations for  $\alpha$  and  $C_P$ .

The contribution  $F^{b,ah}$  has been discussed in detail in Sec. II C. The corresponding free energy  $F^{v,ah}$  was treated in exactly the same manner, i.e., using the UP-TILD approach and the same set of convergence parameters as for the perfect bulk. We ensured the applicability of the UP-TILD procedure to the vacancy by calculating two free-energy points at 900 K for different volumes directly. Further, we find similar  $\lambda$  dependencies for  $F^{b,ah}$  and  $F^{v,ah}$  (Sec. II C 1) and only negligible<sup>36</sup> effects on the vacancy properties when increasing the supercell from  $2^3$  to  $3^3$ .

### III. RESULTS I: INFLUENCE OF THE VARIOUS CONTRIBUTIONS

In this section, we will assess the influence of the various free-energy contributions given in Eq. (1) on selected thermodynamic properties: the heat capacity  $C_P$  at constant pressure, the free energy  $F_P$  at constant pressure, and the expansion coefficient  $\alpha$ . The central results are summarized in Fig. 6 and Table III. All contributions beyond the quasiharmonic contribution can be considered as small perturbations. We therefore discuss the latter in the first place.

#### A. Quasiharmonic approximation and electronic excitations

The *ab initio* calculation of thermodynamic properties within the quasiharmonic approximation is nowadays standard.<sup>3,54–56</sup> Since the main aim here is the accurate description of free-energy contributions beyond the quasiharmonic approximation, a numerical accuracy of well below 1 meV/atom is needed at the melting temperature for the quasiharmonic part. Critical in this regard is the parametrization of the quasiharmonic free-energy surface  $F^{qh}(V, T)$  along the volume. The temperature dependence presents no additional challenge due to the analytical dependence given in Eq. (4). In the following, we test three approximations which are rather convenient since for each of them it is practically sufficient to calculate the phonons at two different volumes.

(a) The volume dependence is parametrized using the linear Grüneisen approximation,<sup>41</sup>

$$-\frac{V}{\omega_q(V)} \frac{\partial \omega_q}{\partial V} = \gamma_q = \text{const}, \quad (26)$$

with the Grüneisen constant  $\gamma_q$ . The index  $q$  runs over the  $q$  vectors inside the first Brillouin zone and the various phonon branches. Solving for  $\omega_q(V)$  yields  $\omega_q(V) = a_q V^{-\gamma_q}$ , with an integration constant  $a_q$ .

(b) The frequencies are assumed to depend linearly on the volume,

$$\partial \omega_q / \partial V = c_q = \text{const}. \quad (27)$$

(c) The free energy is assumed to depend linearly on the volume,

$$\partial F / \partial V = c = \text{const}. \quad (28)$$

Assumption (c) is not equivalent to (b) since the free-energy dependence on the frequencies is strongly nonlinear.

Based on our highly converged free energies for a large number of volume sample points, we are in the position to

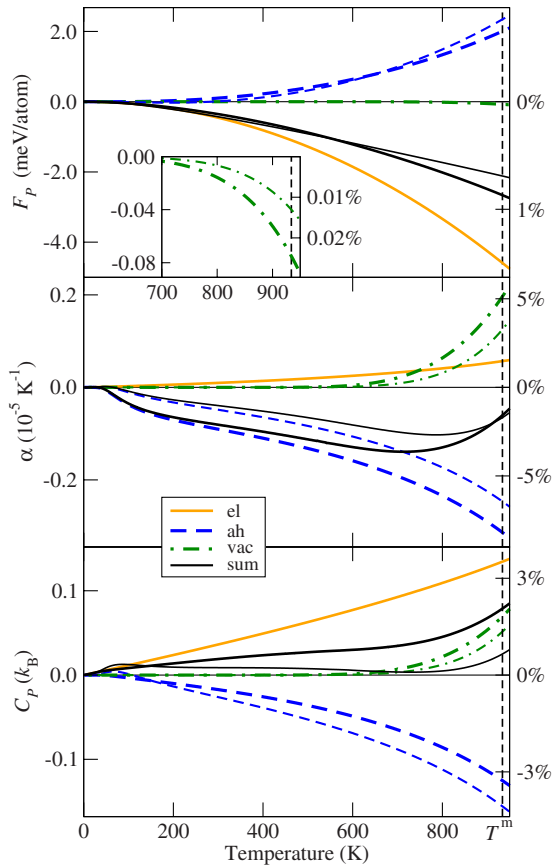


FIG. 6. (Color online) The contribution of the electronic (el), explicitly anharmonic (ah), and vacancy (vac) excitations to the free energy  $F_p$  at constant pressure, the expansion coefficient  $\alpha$ , and the heat capacity  $C_p$  at constant pressure (all quantities at zero pressure). The black solid lines show the sum of all excitations. Thick lines show GGA results. LDA results are either shown as thin lines or coincide with the GGA result. The right axes are scaled with respect to the “full” GGA values at the melting temperature  $T^m$  (indicated by the vertical dashed line) given in Table III. The inset shows an enlargement of the vacancy contribution to  $F_p$  at high temperatures.

check the validity or performance of each of these approximations. We therefore compute the free-energy surface using a polynomial of third order in the volume and the seven explicitly calculated volume points. Extending the polynomial to higher orders has negligible<sup>37</sup> effect on the results. Figure 7 shows the comparison with respect to our target quantities  $\alpha$  and  $C_p$ .

As can be seen, applying approximation (b) yields dramatically wrong  $\alpha$  and  $C_p$  values at temperatures close to the melting point  $T^m$ . At  $T^m$ , they are overestimated by 74% and 21%, respectively. In contrast, approximation (a) yields strong underestimations,  $-27\%$  for  $\alpha$  and  $-7\%$  for  $C_p$ . The best approximation is (c) yielding underestimations of  $-14\%$  for  $\alpha$  and  $-4\%$  for  $C_p$ . However, the remaining error is of the same magnitude as the contributions beyond the quasiharmonic approximation (compare to Table III). In the further analysis, we therefore use the fully converged free-energy surface, i.e., the third-order parametrization along the volume.

TABLE III. Contribution of the quasiharmonic (qh), electronic (el), anharmonic (ah), and vacancy (vac) excitations to the free-energy  $F_p$ , expansion coefficient  $\alpha$ , and heat capacity  $C_p$ . The given values refer to the melting temperature 933 K, zero pressure, LDA, and GGA XC-functional. The relative values refer to the full (qh + ah + el + vac) contribution.

	LDA $F_p$		GGA $F_p$	
	(meV/atom)	(%)	(meV/atom)	(%)
Full	-300.5	100.0	-312.5	100.0
qh	-298.4	99.3	-309.9	99.1
el	-4.4	1.5	-4.6	1.5
ah	2.3	-0.8	2.0	-0.6
vac	0.0	0.0	-0.1	0.0

	LDA $\alpha$		GGA $\alpha$	
	( $10^{-5} \text{ K}^{-1}$ )	(%)	( $10^{-5} \text{ K}^{-1}$ )	(%)
Full	3.68	100.0	3.83	100.0
qh	3.75	101.8	3.89	101.6
el	0.06	1.5	0.06	1.5
ah	-0.25	-6.7	-0.31	-8.1
vac	0.12	3.4	0.20	5.1

	LDA $C_p$		GGA $C_p$	
	( $k_B$ )	(%)	( $k_B$ )	(%)
Full	3.73	100.0	3.83	100.0
qh	3.71	99.3	3.75	97.9
el	0.13	3.5	0.13	3.5
ah	-0.16	-4.2	-0.12	-3.3
vac	0.05	1.4	0.07	1.8

Having constructed a well-defined reference, we can continue to investigate the remaining free-energy contributions. The influence of the electronic excitations on  $F_p$ ,  $\alpha$ , and  $C_p$  is shown in Fig. 6 and Table III. At  $T^m$  the contribution is  $-4.4$  ( $-4.6$ ) meV/atom for LDA (GGA), which is 1.5% with respect to the full free energy. Further, the electronic contribution shifts  $\alpha$  upward by 1.5%, while the largest influence is found for  $C_p$  (3.5%). These values agree with the PAW results from our previous study.<sup>3</sup>

### B. Explicit anharmonicity: Direct *ab initio* calculations and introduction of an analytical model

We now direct our focus on the explicit anharmonicity. As outlined in Sec. I, this is one of the mechanisms proposed in the literature to explain the nonlinear increase in the experimental heat capacity. *Ab initio* calculations of the anharmonic free-energy  $F^{\text{ah}}$  contribution are rather scarce.<sup>42,57</sup> One exception is the seminal work by Vočadlo and Alfè,<sup>42</sup> who determined the melting curve of aluminum under extreme temperatures and pressures. The temperature and pressure region investigated in this work are very different from ours

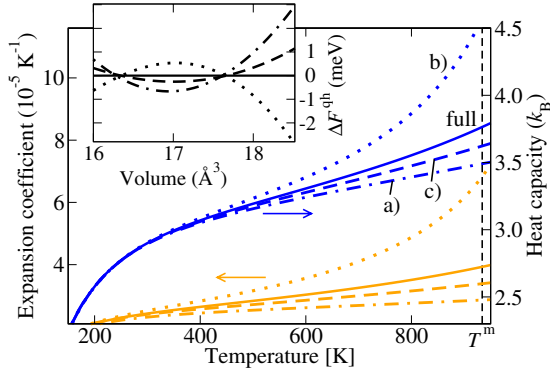


FIG. 7. (Color online) Quasiharmonic expansion coefficient and heat capacity at zero pressure. The solid lines correspond to fully converged quantities. The dotted-dashed/dotted/dashed lines represent quantities based on approximation (a)/(b)/(c) [see Eqs. (26)–(28) for details]. The inset shows the corresponding free energies  $\Delta F^{\text{qh}}$  (per atom) at 900 K referenced to the fully converged free energy. The curves correspond to GGA results. LDA results show the same behavior. The vertical thin dashed line marks the melting temperature  $T^m$ .

so the corresponding anharmonic free energies cannot be used here.

A representative set of our results for  $F^{\text{ah}}$  is shown in Figs. 8 and 9. The figures reveal that  $F^{\text{ah}}$  is positive in the whole region except for a small low-temperature regime, which is likely due to statistical noise. The absolute values close to the melting temperature are  $\approx 2$  meV, which is about 2 orders of magnitude smaller than  $F^{\text{qh}}$ . The volume dependence is positive with a small positive curvature. The temperature dependence has a curvature which goes beyond second order. The results for LDA and GGA are qualitatively similar. Comparing relative  $F^{\text{ah}}$  values, i.e., referenced to the corresponding equilibrium volume, LDA and GGA results differ by an almost constant shift. At 900 K, this shift is  $\approx 0.5$  meV (see Fig. 8).

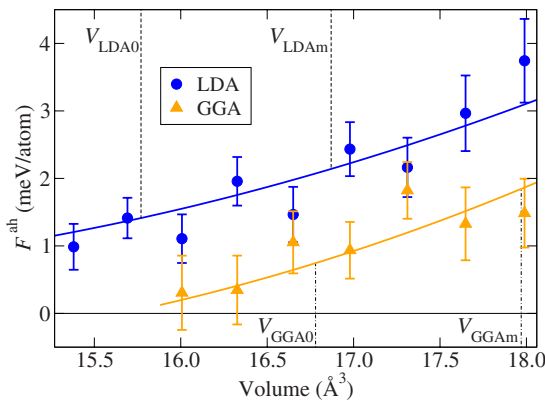


FIG. 8. (Color online) Explicitly anharmonic free energy  $F^{\text{ah}}$  at 900 K for the two investigated XC functionals. The dots/triangles represent the calculated values, while the corresponding vertical lines indicate the standard deviation (Ref. 44). The solid lines are fits using the analytical model (see text). The vertical dashed (dotted-dashed) lines indicate the 0 K (including zero-point vibrations) and melting temperature equilibrium volumes of LDA (GGA),  $V_{\text{LDA}0}$  ( $V_{\text{GGA}0}$ ) and  $V_{\text{LDA}m}$  ( $V_{\text{GGA}m}$ ), respectively.

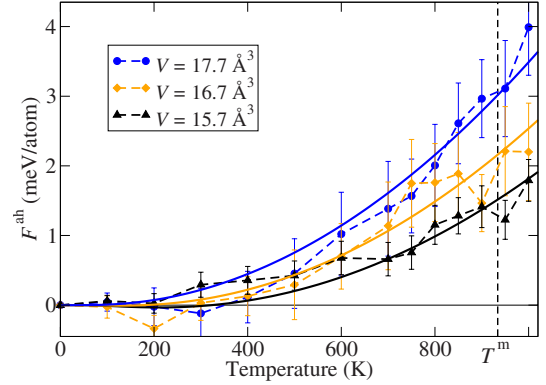


FIG. 9. (Color online) Explicitly anharmonic free energy  $F^{\text{ah}}$  at three different volumes for the LDA functional. The calculated values are represented by the dots/diamonds/triangles. At each point the statistical error is represented by the vertical solid lines. The dashed lines in between are a guide for the eyes and the solid lines are fits using the analytical model (see text). GGA results show the same qualitative dependence. The melting temperature  $T^m$  is indicated by the vertical dashed line.

The anharmonic contribution to the free energy  $F^{\text{ah}}$  has a significant influence on  $\alpha$  and  $C_p$ . Figure 6 shows that  $\alpha$  is shifted downward by  $\approx -7\%$  and  $C_p$  by  $\approx -3.5\%$ . In fact, the negative anharmonic contribution to  $C_p$  cancels the positive contribution from electronic excitations over a large temperature range yielding a close to zero net contribution. For  $\alpha$ , the anharmonic contribution is much stronger (roughly a factor of 5) compared to the electronic one yielding a net decrease in the expansion coefficient. An important conclusion from these results is that explicit anharmonicity cannot be considered as the origin of the nonlinear increase in contrast to current belief. This applies to both the expansion coefficient and the heat capacity. In fact, even the sign is opposite to the one previously assumed: for both quantities, anharmonicity results in a reduction rather than in an increase at high temperatures.

A major source of this unexpected behavior lies in the increase in  $F^{\text{ah}}$  with increasing volume. To verify this statement, we artificially forced  $F^{\text{ah}}(V, T)$  in a separate calculation to be volume independent:  $F^{\text{ah,fix}}(V, T) = F^{\text{ah}}[V(T=0 \text{ K}), T]$ . Note that the explicit temperature dependence is fully included. Replacing the full anharmonic free energy by  $F^{\text{ah,fix}}$  makes the anharmonic contribution to  $\alpha$  practically disappear<sup>36</sup> while the anharmonic contribution to  $C_p$  is reduced by  $\approx 60\%$ .

In order to resolve the physical origin of the positive volume dependence, we developed an approximate analytical model. The key idea is to replace the full phonon spectrum by a single effective frequency and describe anharmonicity by its renormalization. Within this model, the anharmonic free energy is expressed as

$$F^{\text{ah}}(V, T) = F^{\text{qh}}[T; \bar{\omega}^{\text{qh}}(V) + \bar{\omega}^{\text{ah}}] - F^{\text{qh}}[T; \bar{\omega}^{\text{qh}}(V)]. \quad (29)$$

Here,  $\bar{\omega}^{\text{qh}}$  is an effective/averaged quasiharmonic frequency,  $\bar{\omega}^{\text{ah}}$  is the renormalization shift due to anharmonicity, and  $F^{\text{qh}}(T; \bar{\omega})$  is obtained from an adapted version of Eq. (4),

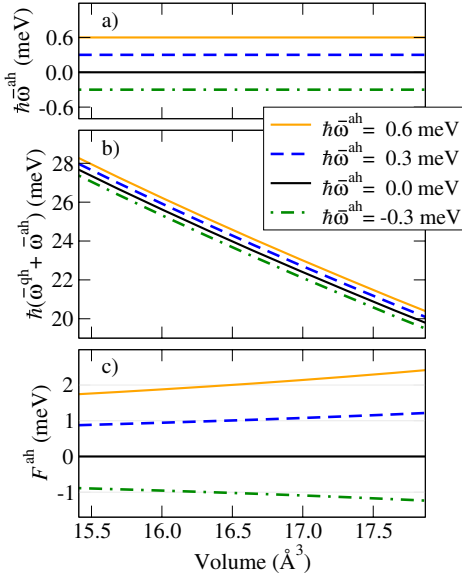


FIG. 10. (Color online) Illustration of the analytical model (see text) describing the origin of the anharmonic free energy. (a) Volume independent anharmonic frequency  $\bar{\omega}^{\text{ah}}$ . (b) Effective frequency resulting from the sum of the quasiharmonic frequency  $\bar{\omega}^{\text{qh}}$  and  $\bar{\omega}^{\text{ah}}$ . (c) Model anharmonic free energy  $F^{\text{ah}}$  at the melting temperature as obtained from Eq. (29) and the frequencies from (b).

$$F^{\text{qh}}(T; \bar{\omega}) = k_B T \ln \left[ 1 - \exp\left(-\frac{\hbar\bar{\omega}}{k_B T}\right) \right]. \quad (30)$$

In principle,  $\bar{\omega}^{\text{qh}}(V)$  could be obtained from the Grüneisen parameter by means of the Grüneisen approximation [Eq. (26)]. However for consistency, we use our explicitly calculated quasiharmonic phonon spectrum  $\omega^{\text{qh}}(V)$ . We therefore calculate  $\bar{\omega}^{\text{qh}}(V) = 1/(3N_q) \sum_q^{3N_q} \omega_q^{\text{qh}}(V)$ , where  $q$  runs over the  $N_q$  exact  $q$  vectors inside the first Brillouin zone and the various phonon branches. Figure 10(b) (black solid line) shows the volume dependence of  $\bar{\omega}^{\text{qh}}$ . The anharmonic shift  $\bar{\omega}^{\text{ah}}$  in Eq. (29) accounts for the anharmonic free energy. Tests based on our *ab initio* data showed that, in order to capture the essential qualitative features, it is sufficient to assume  $\bar{\omega}^{\text{ah}}$  to be volume independent.

The magnitude of this volume independent shift is used as a free parameter to fit to the *ab initio* data and to explore the physics embodied in the model. The resulting anharmonic free energy for three different  $\bar{\omega}^{\text{ah}}$  is shown in Fig. 10(c). If we assume a negative shift,  $F^{\text{ah}}$  is negative and shows a negative volume dependence. Thus, to reproduce the positive anharmonic free energy observed in the *ab initio* results, the renormalization shift must be positive, i.e., the renormalized phonons must be blueshifted in average. By introducing linear volume and temperature dependence<sup>58</sup> in  $\bar{\omega}^{\text{ah}}$  also a good quantitative description of the full volume and temperature dependence of the anharmonic free-energy surface is achieved. The quality of this approach is shown in Figs. 8 and 9 (solid lines). It was also successfully employed for the parametrization of the corresponding vacancy contribution (Fig. 12).

The key result we obtain from this analysis is that the vibrational free energy and hence the major part of the ther-

modynamics of aluminum at high temperatures, up to the melting point, can be well described by renormalized phonon frequencies. Compared to the quasiharmonic frequencies, the renormalized frequencies are in average energetically harder (blueshifted) but exhibit a similar volume dependence.

### C. Vacancies: Electronic, quasiharmonic, and anharmonic excitations

We now discuss the remaining mechanism proposed as source for the nonlinear increase in the experimental heat capacity: the thermal formation of point defects. Specifically, monovacancies are believed to be the dominating point defects, while the influence of self-interstitials and divacancies is negligible due to the high formation energy ( $\approx 3.4$  eV) (Ref. 59) and a negative binding energy,<sup>49</sup> respectively. Starting with the seminal work by Gillan,<sup>47</sup> monovacancies in aluminum have been studied extensively in the past by *ab initio* techniques.<sup>48,49,59–61</sup> However, the focus has been mainly on  $T=0$  K properties. Finite temperature effects, except for the configurational entropy, have not been included. One exception is a combined study<sup>49</sup> where the  $T=0$  K energetics and the harmonic contribution have been determined by DFT while the remaining finite temperature effects have been obtained by employing empirical potentials (referred to as the ai/ep approach in the following).

Our results for the full [i.e., including all free-energy terms in Eq. (24)] contribution of the vacancies to  $F_p$ ,  $\alpha$ , and  $C_p$  are shown in Fig. 6. The contribution to  $F_p$  is negative and rather small,  $\approx -0.1$  meV/atom at  $T^m$ , i.e., well below 0.1% of the quasiharmonic reference. Surprisingly, despite the small free-energy contribution due to vacancies, they substantially contribute to  $\alpha$  and  $C_p$  in the temperature window from  $\approx 700$  K up to  $T^m$ . This effect is related to the strong nonlinear decrease in this free-energy contribution with temperature. For both quantities,  $\alpha$  and  $C_p$ , the anharmonic contribution is positive and amounts to  $\approx 5\%$  and  $\approx 2\%$  of the quasiharmonic reference at  $T^m$ , respectively.

With the fully *ab initio* calculated results at hand, we have a reference against which the performance or accuracy of previously suggested empirical approaches to estimate the effect of vacancies can be tested. One such empirical estimation<sup>16</sup> starts from the following expression for the vacancy contribution to the vacancy heat capacity  $C^{\text{vac}}$ ,

$$C^{\text{vac}} = k_B \left( \frac{E^f}{k_B T} \right)^2 \exp\left(-\frac{E^f - TS^f}{k_B T}\right). \quad (31)$$

Here,  $E^f$  is the formation energy, which was set to the experimental value of 0.66 eV from Ref. 64. Further, the entropy of formation  $S^f$  was estimated to be  $1.4k_B$  based on experimental heat capacity data and empirical potential calculations of the heat capacity excluding vacancy contributions. Using these values, Shukla *et al.*<sup>16</sup> estimated an increase in  $C_p$  of  $0.08k_B$  at  $T^m$  due to vacancies. This approximate value based on experimental input is in surprisingly good agreement with our explicitly calculated values of  $0.05k_B$  for LDA and  $0.08k_B$  for GGA.

We finally turn to the comparison with the ai/ep approach, discuss the validity of the assumption given in Eq. (21), and

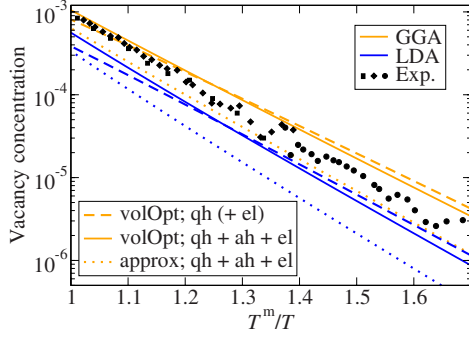


FIG. 11. (Color online) Equilibrium vacancy concentration as a function of the inverse temperature multiplied by the melting temperature  $T^m$ . Results for the two investigated exchange-correlation functionals, LDA, and GGA, are shown. The solid lines correspond to a volume-optimized (volOpt) calculation, i.e., one which is based on solving the coupled system of Eqs. (16)–(19), with all free-energy terms included in Eq. (24). The dashed lines correspond to a volume-optimized calculation excluding the anharmonic free-energy terms,  $F^{b,ah}$  and  $F^{v,ah}$ , in Eq. (24). The dashed lines also correspond to a volume-optimized calculation excluding the anharmonic,  $F^{b,ah}$  and  $F^{v,ah}$ , and electronic,  $\bar{F}^{b,el}$  and  $\bar{F}^{v,el}$  (indicated by the parentheses enclosing the electronic contribution in the legend) terms in Eq. (24). The dotted lines correspond to a calculation based on the approximation (approx) Eq. (21) and including all free-energy terms. The squares indicate experimental values from Ref. 62 (differential dilatometry). The diamonds/circles indicate experimental values from Ref. 63 (differential dilatometry/positron annihilation).

analyze the various contributions to the vacancy results. Figure 11 summarizes the calculated vacancy concentration as a function of temperature employing the full formalism and applying various approximations. A comparison with experiment (squares, diamonds, and dots) shows overall a good agreement: using the full approach, i.e., including all free-energy contributions in Eq. (24) and applying the optimized volume formalism [Eqs. (16)–(19)], LDA and GGA are very close to experiment and form lower and upper bounds, respectively. This behavior of LDA/GGA to form bounds to experimental data is similar to what has been reported in previous studies.<sup>3,65</sup> To allow a more quantitative analysis of the various approximations and to compare with previous studies, we deduced from the temperature dependence of the vacancy concentrations the formation energy  $E^f$  and entropy  $S^f$ . The data compiled in Table IV show a good agreement of our full approach with the ai/ep approach.<sup>17</sup> Table IV also reveals the influence of the various excitation mechanisms on the vacancy properties: we find that the electronic contribution is negligible. In contrast, the anharmonic contribution to the vacancies has a large influence on the entropy of formation increasing it from  $0.2k_B$  ( $0.1k_B$ ) to  $2.2k_B$  ( $1.5k_B$ ) for LDA (GGA). This strong influence can be traced back to the temperature dependence of the explicitly anharmonic free-energy surface for the vacancy cell. From Fig. 12, it becomes apparent that the anharmonic free energy is concave at higher temperatures in contrast to the convex temperature dependence of the perfect crystal anharmonic free energy (Fig. 9). The corresponding difference favors the creation of vacancies.

TABLE IV. The formation energy  $E^f$  and entropy of formation  $S^f$  for various approaches and combinations of the free-energy contributions used for the calculation of the vacancy properties. ai/ep indicates values for the coupled *ab initio*–empirical potentials approach from Ref. 49. The further values (also the experimental) are obtained by fitting the vacancy concentrations over the temperature range given in Fig. 11 to the function  $\exp[-(E^f - TS^f)/k_B T]$ . The notation is as in Fig. 11.

	$E^f$ (eV)		$S^f$ ( $k_B$ )	
	LDA	GGA	LDA	GGA
volOpt; qh	0.65	0.58	0.2	0.1
volOpt; qh+el	0.65	0.58	0.2	0.1
volOpt; qh+ah+el	0.78	0.68	2.2	1.5
Approx; qh+ah+el	0.85	0.75	2.5	1.9
ai/ep <sup>a</sup>	0.78	0.61	1.6	1.3
Experiment	0.75		2.4	

<sup>a</sup>Reference 49.

#### IV. RESULTS II: COMPARISON BETWEEN THEORY AND EXPERIMENT

So far, we have discussed all terms of Eq. (1) separately. Now, we are able to construct the full free-energy surface  $F(V, T)$  and calculate the final thermodynamic quantities  $F_P$ ,  $\alpha$ , and  $C_P$  including all excitations. These quantities can be directly compared to experiment. For instance, the free energy  $F_P$  at constant pressure can be compared to CALPHAD<sup>66</sup> data. Figure 13 shows that the LDA results overestimate the CALPHAD free energy by 4.9 meV/atom at the melting temperature, while the GGA results underestimate it by  $-4.7$  meV/atom, i.e., by a similar magnitude. These error bars have a similar magnitude and show the same trends as the ones found in Ref. 3 for a wide range of metals.

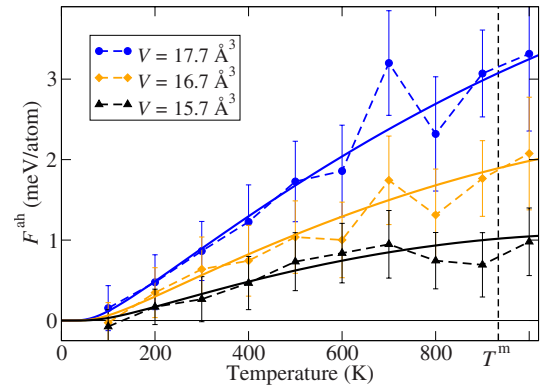


FIG. 12. (Color online) Explicitly anharmonic free energy  $F^{ah}$  of the vacancy calculation at three different volumes for the LDA functional. The dots/diamonds/triangles represent the calculated values. At each point the statistical error is represented by the vertical solid lines. The dashed lines in between are guides for the eyes and the solid lines are fits using the analytical model (see Sec III B). GGA results show the same qualitative dependence. The melting temperature  $T^m$  is given by the vertical dashed line.

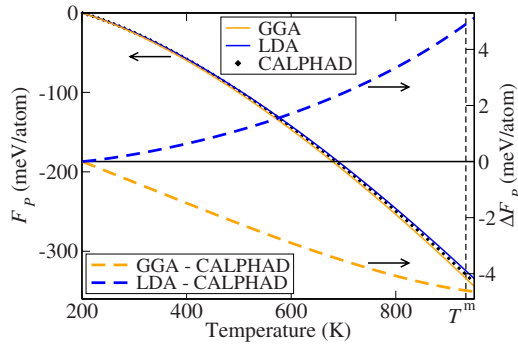


FIG. 13. (Color online) Free energy  $F_P$  at constant pressure for the two investigated exchange-correlation functionals: LDA and GGA, in comparison with CALPHAD results (obtained using THERMOCALC version  $Q$  and the “PURE4-SGTE pure elements database”). Both the *ab initio* and the CALPHAD data were shifted to zero at  $T = 200$  K. For the difference free energy  $\Delta F_P$  the CALPHAD data are taken as a reference at each temperature. The melting temperature  $T^m$  is given by the vertical dashed line.

Next, we compare the *ab initio* computed isobaric heat capacity  $C_P$  with experiment. As shown in Fig. 14, a good agreement for the low-temperature heat capacity between theory and experiment is found. In the temperature region up to  $\approx 600$  K, the majority of the experimental data agrees well with our *ab initio* data. Note also that the heat capacity is shown on a rather fine scale to better visualize the deviations. Above 600 K, there is a large scatter in the experimental data making a fair comparison with our *ab initio* data difficult. A general trend is that almost all experiments performed later than 1950 (solid squares in Fig. 14) show a steeper increase toward the melting temperature making the *ab initio* data a lower bound. With the presently available experimental data, a final conclusion whether the remaining small deviation ( $\approx 0.2k_B$  at  $T^m$ ) is due to the limited accuracy of presently available exchange-correlation functionals or due to errors in the experimental data is not possible. The fact that the *ab initio* data are a lower bound to the scattered

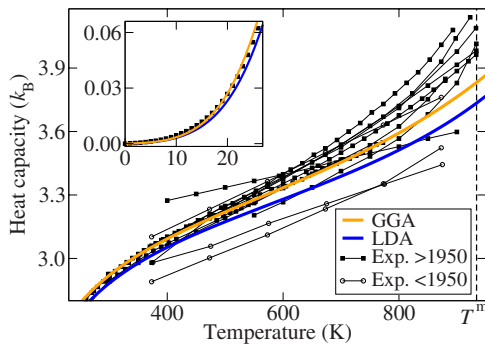


FIG. 14. (Color online) Heat capacity at constant pressure for the two investigated exchange-correlation functionals, LDA and GGA, in comparison with experiment. The melting temperature  $T^m$  is given by the vertical dashed line. Experimental data older than 1950 are indicated by the open circles (Refs. 7–9). The remaining experimental data are indicated by the filled squares (Refs. 2, 5, 6, and 10–15). The inset shows the low-temperature region with experimental data from Ref. 6.

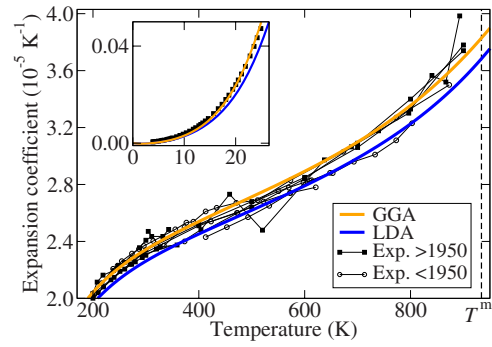


FIG. 15. (Color online) Thermal expansion coefficient for the two investigated exchange-correlation functionals, LDA and GGA, in comparison with experiment. The melting temperature  $T^m$  is given by the vertical dashed line. Experimental data older than 1950 are indicated by the open circles (Refs. 67–70). The remaining experimental data are indicated by the filled squares (Refs. 71–76). The inset shows the low-temperature region with experimental data from Ref. 77.

experimental data suggests that there are additional sources for the heat capacity in the experimental measurements, however of varying influence. Possible sources are imperfections within the sample, such as dislocations, grain boundaries, impurities, etc. Systematic deviations can also be caused by the experimental setup, such as for instance the sample holder. In particular, the cubic dependence of the radiant heat-exchange coefficient on the temperature is an experimental challenge.<sup>14</sup>

In contrast to the heat capacity, which is experimentally difficult to measure and shows large scatter in the data, the temperature dependence of the thermal expansion coefficient requires the determination of interatomic distances which can be obtained by x-ray measurements with high precision. The experimental together with our *ab initio* data are shown in Fig. 15. The *ab initio* values agree with the experimental data over the full temperature range up to the melting temperature  $T^m$ . Even details such as the curvature of  $\alpha$  at high temperatures are well reproduced. It is important to note that only the combined interplay of the electronic, quasiharmonic, anharmonic, and vacancy contribution (black solid lines in Fig. 6) provides this agreement. Particularly important for the steep increase close to the melting temperature is the strongly nonlinear increase due to vacancy formation.

## V. CONCLUSIONS

In the present study, we have described an integrated fully *ab initio* approach that allows the determination of all relevant free-energy contributions of nonmagnetic elementary crystals with a numerical accuracy better than 1 meV/atom. The high accuracy has been achieved by extensive and systematic convergence checks together with methodological advancements. Key findings and methods for the relevant free-energy contributions are briefly summarized in the following:

*Quasiharmonicity.* This contribution strongly dominates the thermodynamic properties (Table III). Separation of the further (much smaller) contributions, in particular the anharmonicity, requires a highly converged quasiharmonic free energy with respect to plane-wave cutoff,  $k$  sampling (Sec. II B), and the volume parametrization (Sec. III A). For the latter, we find that a linear Grüneisen approximation is not sufficient (Fig. 7). For the vacancies, great care has to be taken regarding the  $q$  sampling which needs to be performed consistently for the perfect bulk and the vacancy supercell (Sec. II D 2). We propose a simple correction scheme [Eq. (25)] that ensures a consistent treatment but retains the advantage of a dense  $q$  sampling for the perfect bulk.

*Anharmonicity.* The key challenge here is an efficient sampling of the configuration space. A statistically converged sampling using a direct molecular dynamics approach requires  $\approx 10^7$  steps to achieve the desired accuracy. We have developed a hierarchical scheme (UP-TILD; Sec. II C 2) that efficiently coarse grains the configuration space and requires at the finest level with highly converged DFT parameters only 50,  $\dots$ , 100 configurations.<sup>78</sup> This scheme together with an analytical model describing the temperature dependent phonon renormalization (Sec. II B; Fig. 10) allowed us to compute a smooth anharmonic free-energy surface  $F^{\text{ah}}(V, T)$ . The smoothness guarantees that derived quantities such as the isobaric heat capacity or the expansion coefficient can be calculated with sufficient accuracy (Fig. 6).

*Vacancies.* Two important points have been identified here: first, a consistent scheme to treat the quasiharmonic contribution of the perfect bulk and vacancy supercell is crucial (see above). Second, the usually applied separation of the vacancy contribution by means of a formation free energy, which is based on the assumption of a constant vacancy supercell volume [Eq. (21)], needs to be abandoned to achieve the desired accuracy (Fig. 11). We have therefore derived a set of coupled equations [Eqs. (16)–(19)] to treat the vacancy contribution with a self-consistently optimized vacancy cell volume (Sec. II D 1).

Using the integrated approach, we calculated the free-energy surface  $F(V, T)$  for aluminum and derived the isobaric heat capacity and the expansion coefficient. Generally, a surprisingly good agreement between our fully *ab initio* data and experiment is found (Figs. 14 and 15). For the high temperature heat capacity, the strong scatter in the experimental data inhibits a final conclusion regarding the accuracy of the *ab initio* results. We find however that the *ab initio* data provide a lower bound to the experimental results.

Based on a systematic study of the various free-energy contributions, we were able to address the fundamental question which excitation mechanism dominates thermodynamic quantities close to the melting point. This issue has been raised first by Born and Brody<sup>1</sup> almost a century ago and has been heavily debated since then in both experimental and theoretical studies.<sup>4,5,16,79</sup> Analyzing the various free-energy contributions (Fig. 6), we find that in contrast to common belief the explicit anharmonicity gives rise to a negative contribution to the isobaric heat capacity. We can therefore conclude that only the vacancies, for which we find a significant anharmonic contribution to the entropy of formation, give rise to the steep positive increase in the heat capacity as observed in experiment.

We believe that the achievable numerical accuracy of this approach will open a number of interesting research topics. This accuracy is crucial to systematically check the performance of recently proposed alternative exchange-correlation functionals with respect to their ability in describing finite temperature material properties. Other possible applications are the calculation of phase transitions and subsequently thermodynamic phase diagrams.

#### ACKNOWLEDGMENTS

We acknowledge financial support by the DFG within the SFB 761 *Stahl ab initio* and stimulating discussions with B. Hallstedt (RWTH-Aachen) and R. Schmidt-Fetzer (TU Clausthal).

<sup>1</sup>M. Born and E. Brody, *Z. Phys.* **6**, 132 (1921).

<sup>2</sup>T. E. Pochapsky, *Acta Metall.* **1**, 747 (1953).

<sup>3</sup>B. Grabowski, T. Hickel, and J. Neugebauer, *Phys. Rev. B* **76**, 024309 (2007).

<sup>4</sup>Y. Kraftmakher, *Phys. Rep.* **299**, 79 (1998).

<sup>5</sup>C. R. Brooks and R. E. Bingham, *J. Phys. Chem. Solids* **29**, 1553 (1968).

<sup>6</sup>D. A. Ditmars, C. A. Plint, and R. C. Shukla, *Int. J. Thermophys.* **6**, 499 (1985).

<sup>7</sup>E. D. Eastman, A. M. Williams, and T. F. Young, *J. Am. Chem. Soc.* **46**, 1178 (1924).

<sup>8</sup>S. Umino, *Sci. Rep. Tohoku Imp. Univ., Ser. 1* **15**, 597 (1926) (cited from Ref. 14).

<sup>9</sup>A. Avramescu, *Z. Tech. Phys. (Leipzig)* **20**, 213 (1939).

<sup>10</sup>R. A. McDonald, *J. Chem. Eng. Data* **12**, 115 (1967).

<sup>11</sup>A. J. Leadbetter, *J. Phys. C* **1**, 1481 (1968).

<sup>12</sup>U. Schmidt, O. Vollmer, and R. Kohlhaas, *Z. Naturforsch. A* **25A**, 1258 (1970).

<sup>13</sup>D. I. Marchidan and M. Ciopec, *Rev. Roum. Chim.* **15**, 1005 (1970) (cited from Ref. 14).

<sup>14</sup>P. D. Desai, *Int. J. Thermophys.* **8**, 621 (1987).

<sup>15</sup>Y. Takahashi, T. Azumi, and Y. Sekine, *Thermochim. Acta* **139**, 133 (1989).

<sup>16</sup>R. C. Shukla, C. A. Plint, and D. A. Ditmars, *Int. J. Thermophys.* **6**, 517 (1985).

<sup>17</sup>M. Forsblom, N. Sandberg, and G. Grimvall, *Phys. Rev. B* **69**, 165106 (2004).

<sup>18</sup>Forsblom *et al.* (Ref. 17) employed three potential parametrizations and obtained at the melting temperature an anharmonic contribution to the fixed volume heat capacities of  $0.06k_B$ ,  $0.03k_B$ , and  $-0.05k_B$  (cf. Fig. 2 in Ref. 17;  $k_B$ : Boltzmann's constant). Shukla *et al.* (Ref. 16) estimated a vacancy contribution to the fixed volume heat capacity of  $0.08k_B$  at the melting point [cf. Eq. (15) and Fig. 4 in Ref. 16 and our discussion in Sec. III C].

<sup>19</sup>X. Gonze *et al.*, *Comput. Mater. Sci.* **25**, 478 (2002).

- <sup>20</sup>X. Gonze *et al.*, *Z. Kristallogr.* **220**, 558 (2005).
- <sup>21</sup>S. Boeck *et al.*, <http://www.sphinxlib.de/>
- <sup>22</sup>L. Ismer, Ph.D. thesis, University of Paderborn, 2008.
- <sup>23</sup>M. Fuchs and M. Scheffler, *Comput. Phys. Commun.* **119**, 67 (1999).
- <sup>24</sup>D. R. Hamann, *Phys. Rev. B* **40**, 2980 (1989).
- <sup>25</sup>P. E. Blöchl, *Phys. Rev. B* **50**, 17953 (1994).
- <sup>26</sup>G. Kresse and J. Furthmüller, *Phys. Rev. B* **54**, 11169 (1996).
- <sup>27</sup>G. Kresse and D. Joubert, *Phys. Rev. B* **59**, 1758 (1999).
- <sup>28</sup>P. Blaha, K. Schwarz, G. Madsen, D. Kvasnicka, and J. Luitz, *WIEN2k, An Augmented Plane Wave+Local Orbitals Program for Calculating Crystal Properties* (Technische Universität, Wien, Austria, 2001).
- <sup>29</sup>D. M. Ceperley and B. J. Alder, *Phys. Rev. Lett.* **45**, 566 (1980).
- <sup>30</sup>J. P. Perdew and A. Zunger, *Phys. Rev. B* **23**, 5048 (1981).
- <sup>31</sup>J. P. Perdew, K. Burke, and M. Ernzerhof, *Phys. Rev. Lett.* **77**, 3865 (1996).
- <sup>32</sup>F. D. Murnaghan, *Proc. Natl. Acad. Sci. U.S.A.* **30**, 244 (1944).
- <sup>33</sup>F. Birch, *Phys. Rev.* **71**, 809 (1947).
- <sup>34</sup>P. Vinet, J. Ferrante, J. H. Rose, and J. R. Smith, *J. Geophys. Res., [Solid Earth Planets]* **92**, 9319 (1987).
- <sup>35</sup>R. E. Cohen, O. Gülseren, and R. J. Hemley, *Am. Mineral.* **85**, 338 (2000).
- <sup>36</sup>We call an error or an effect negligible if it is below 1.0% for  $\alpha$  and below 0.5% for  $C_p$  (Ref. 37).
- <sup>37</sup>As a reference for the relative values for  $\alpha$  and  $C_p$ , we take the final quantities containing all contributions at the melting temperature of aluminum (933 K) and at zero pressure. LDA:  $\alpha = 3.68 \times 10^{-5} \text{ K}^{-1}$  and  $C_p = 3.73 k_B$ ; GGA:  $\alpha = 3.83 \times 10^{-5} \text{ K}^{-1}$  and  $C_p = 3.83 k_B$  (see also Table III).
- <sup>38</sup>N. D. Mermin, *Phys. Rev.* **137**, A1441 (1965).
- <sup>39</sup>X. Gonze, *Phys. Rev. B* **55**, 10337 (1997).
- <sup>40</sup>X. Gonze and C. Lee, *Phys. Rev. B* **55**, 10355 (1997).
- <sup>41</sup>D. C. Wallace, *Thermodynamics of Crystals* (Dover, New York, 1998).
- <sup>42</sup>L. Vočadlo and D. Alfè, *Phys. Rev. B* **65**, 214105 (2002).
- <sup>43</sup>G. J. Ackland, *J. Phys.: Condens. Matter* **14**, 2975 (2002).
- <sup>44</sup>The correlation time (approximately equal to ten MD steps) is obtained from the correlation coefficient (Ref. 80). The standard deviation is then calculated using the *stratified systematic sampling* (Ref. 80). Note that, in the case of the UP-TILD method, the standard deviation due to the upsampling [Eq. (8); here the correlation time is zero] needs to be added to the standard deviation from the MD run performed on the set of low-converged parameters.
- <sup>45</sup>As a reference, we take here and in the following an AMD Opteron with a clock speed of 2.4 GHz.
- <sup>46</sup>This equation may be considered the first-order contribution in the free-energy perturbation approach, as applied, e.g., in S. Angioletti-Uberti, M. Asta, M. W. Finnis, and P. D. Lee, *Phys. Rev. B* **78**, 134203 (2008).
- <sup>47</sup>M. J. Gillan, *J. Phys.: Condens. Matter* **1**, 689 (1989).
- <sup>48</sup>R. Benedek, L. H. Yang, C. Woodward, and B. I. Min, *Phys. Rev. B* **45**, 2607 (1992).
- <sup>49</sup>K. M. Carling, G. Wahnström, T. R. Mattsson, N. Sandberg, and G. Grimvall, *Phys. Rev. B* **67**, 054101 (2003).
- <sup>50</sup>To perform vacancy calculations in practice, it is often indispensable to apply a generalized version of the described correction scheme:  $F = \tilde{F} - F^b + F_{\text{best}}^b$ . Here,  $\tilde{F}$  refers to a free energy calculated using consistent parameters for the perfect bulk, denoted as  $F^b$ , and the vacancy cell. Further,  $F_{\text{best}}^b$  is the perfect bulk free energy calculated using the best convergence parameters. The correction is important for the final thermodynamic quantities (Figs. 14 and 15) but does not affect vacancy related properties such as the concentration (Fig. 11) since the latter are obtained directly from  $\tilde{F}$ .
- <sup>51</sup>K. Parlinski, Z. Q. Li, and Y. Kawazoe, *Phys. Rev. Lett.* **78**, 4063 (1997).
- <sup>52</sup>G. Kresse, J. Furthmüller, and J. Hafner, *Europhys. Lett.* **32**, 729 (1995).
- <sup>53</sup>D. Alfè, G. D. Price, and M. J. Gillan, *Phys. Rev. B* **64**, 045123 (2001).
- <sup>54</sup>A. Debernardi, M. Alouani, and H. Dreysse, *Phys. Rev. B* **63**, 064305 (2001).
- <sup>55</sup>A. A. Quong and A. Y. Liu, *Phys. Rev. B* **56**, 7767 (1997).
- <sup>56</sup>A. Siegel, K. Parlinski, and U. D. Wdowik, *Phys. Rev. B* **74**, 104116 (2006).
- <sup>57</sup>D. Alfè, G. A. de Wijs, G. Kresse, and M. J. Gillan, *Int. J. Quantum Chem.* **77**, 871 (2000).
- <sup>58</sup>We use  $\hbar\bar{\omega}^{\text{ah}} = a + bT + cV$  and obtain the following fitting parameters: LDA:  $a = -2.6 \text{ meV}$ ,  $b = 9.9 \times 10^{-4} \text{ meV/K}$ , and  $c = 0.15 \text{ meV/\AA}^3$ ; GGA:  $a = -4.5 \text{ meV}$ ,  $b = 3.1 \times 10^{-4} \text{ meV/K}$ , and  $c = 0.27 \text{ meV/\AA}^3$ .
- <sup>59</sup>P. J. H. Denteneer and J. M. Soler, *J. Phys.: Condens. Matter* **3**, 8777 (1991).
- <sup>60</sup>A. De Vita and M. J. Gillan, *J. Phys.: Condens. Matter* **3**, 6225 (1991).
- <sup>61</sup>K. M. Carling, G. Wahnström, T. R. Mattsson, A. E. Mattsson, N. Sandberg, and G. Grimvall, *Phys. Rev. Lett.* **85**, 3862 (2000).
- <sup>62</sup>R. O. Simmons and R. W. Balluffi, *Phys. Rev.* **117**, 52 (1960).
- <sup>63</sup>Th. Hehenkamp, *J. Phys. Chem. Solids* **55**, 907 (1994).
- <sup>64</sup>W. Triftshäuser, *Phys. Rev. B* **12**, 4634 (1975).
- <sup>65</sup>S. Narasimhan and S. de Gironcoli, *Phys. Rev. B* **65**, 064302 (2002).
- <sup>66</sup>L. Kaufman and H. Bernstein, *Computer Calculation of Phase Diagrams* (Academic, New York, 1970).
- <sup>67</sup>K. Honda and Y. Okubo, *Sci. Rep. Tohoku Imp. Univ., Ser 1* **13**, 101 (1924) (cited from Ref. 72).
- <sup>68</sup>F. L. Uffelmann, *Philos. Mag.* **10**, 633 (1930) (cited from Ref. 72).
- <sup>69</sup>A. J. C. Wilson, *Proc. Phys. Soc.* **54**, 487 (1942).
- <sup>70</sup>F. C. Nix and D. MacNair, *Phys. Rev.* **60**, 597 (1941).
- <sup>71</sup>P. D. Pathak and N. G. Vasavada, *J. Phys. C* **3**, L44 (1970) (cited from Ref. 72).
- <sup>72</sup>Y. S. Touloukian, R. K. Kirby, R. E. Taylor, and P. D. Desai, *Thermal Expansion: Metallic Elements and Alloys*, Thermophysical Properties of Matter Vol. 12 (Plenum, New York, 1975).
- <sup>73</sup>F. R. Kroeger and C. A. Swenson, *J. Appl. Phys.* **48**, 853 (1977).
- <sup>74</sup>B. von Guérard, H. Peisl, and R. Zitzmann, *Appl. Phys.* **3**, 37 (1974). Numerical differentiation of the given experimental expansion data; strongly scattering points were taken out.
- <sup>75</sup>P. G. Strelkov and S. I. Novikova, *Prib. Tekh. Eksp.* **5**, 105 (1957) (cited from Ref. 72).
- <sup>76</sup>R. M. Nicklow and R. A. Young, *Phys. Rev.* **129**, 1936 (1963) (cited from Ref. 72).
- <sup>77</sup>K. O. McLean, Ph.D. thesis, Iowa State University, 1969 (cited from Ref. 72).
- <sup>78</sup>An interesting advancement of the UP-TILD approach would be a combination with an optimized reference potential: it is not

obligatory to use the quasiharmonic potential as the reference potential for the thermodynamic integration as long as the difference between the used and quasiharmonic potential is accounted for at the end of the anharmonic free-energy calculation. Therefore, an artificial reference potential can be constructed which yields an optimum statistical convergence and reduces the

number of molecular dynamics steps. An example for such an optimized reference is inverse power potentials presented in Ref. [42](#).

<sup>79</sup>R. C. Shukla and C. A. Plint, *Int. J. Thermophys.* **1**, 299 (1980).

<sup>80</sup>J. M. Haile, *Molecular Dynamics Simulation: Elementary Methods* (Wiley, New York, 1997), p. 79f.